

Gluon-fusion induced diboson production in the SMEFT

Alejo N. Rossia,^a Marion O. A. Thomas^{a,*} and Eleni Vryonidou^a

^a*Dept. of Physics and Astronomy, University of Manchester,
Oxford Road, Manchester M13 9PL, UK*

*E-mail: alejo.rossia@manchester.ac.uk, marion.thomas@manchester.ac.uk,
eleni.vryonidou@manchester.ac.uk*

Precision measurements of diboson production at the LHC is an important probe of deviations from the Standard Model. The gluon-fusion channel of this process offers a connection between the Higgs and top sectors. We study in a systematic way gluon-induced diboson production in the Standard Model Effective Field Theory, with a focus on double Z and associated ZH production. We compute the helicity amplitudes of these processes at one loop and with up to one insertion of a dimension-6 operator and we study their high-energy limit in order to identify which operators in each channel lead to growths with energy and for which helicity configurations. In addition we perform a phenomenological study of ZH production, including both quark and gluon initial states. We show that for some top operators the gluon-induced channel can offer competitive sensitivity to constraints obtained from top quark production processes.

ARXIV EPRINT: [2306.09963](https://arxiv.org/abs/2306.09963)

*The European Physical Society Conference on High Energy Physics (EPS-HEP2023)
21-25 August 2023
Hamburg, Germany*

*Speaker

1. Introduction

Diboson production from gluon fusion, ie. $gg \rightarrow HH, ZH, ZZ, WW$, is a key channel to study and constrain Higgs and top quark properties as the four processes are mediated by top quark loops. Additionally, the Higgs trilinear coupling can be probed through double Higgs production due to the presence of a Higgs boson in the s-channel. This s-channel Higgs boson is also present in ZZ/WW production and since the cross-sections of these processes depend on the Higgs width in the on-shell region but not in the off-shell one, this has enabled precise measurements of the Higgs width from LHC data [1, 2].

Diboson production can be studied in the Standard Model Effective Field Theory (SMEFT) framework, which extends the SM Lagrangian to higher dimensional operators with an expansion in energy:

$$\mathcal{L}_{\text{SMEFT}} = \mathcal{L}_{\text{SM}} + \sum_{d=5}^{\infty} \sum_k \frac{c_k}{\Lambda^{d-4}} \mathcal{O}_k^{(d)} \quad (1)$$

where each operator $\mathcal{O}_k^{(d)}$ has energy dimension (d), c_k is the corresponding dimensionless Wilson coefficient (WC), and the series converges as long as the typical energy of the process obeys $E/\Lambda \ll 1$. The leading deviations with respect to the SM of relevance for collider physics are generated by operators of dimension 6, on which we focus. We use the Warsaw basis of SMEFT operators along with a $U(2)_q \times U(3)_d \times U(2)_u \times (U(1)_\ell \times U(1)_e)^3$ flavour assumption and the operator definitions from the SMEFTatNLO model [3, 4]. In these proceedings we focus on a subset of relevant operators entering in ZZ and ZH production, which is presented in Table 1.

Gauge operators			2-fermion operators		
\mathcal{O}_i	c_i	Definition	\mathcal{O}_i	c_i	Definition
$\mathcal{O}_{\varphi G}$	$c_{\varphi G}$	$\left(\varphi^\dagger \varphi - \frac{v^2}{2}\right) G_A^{\mu\nu} G_{\mu\nu}^A$	$\mathcal{O}_{\varphi t}$	$c_{\varphi t}$	$i(\varphi^\dagger \overleftrightarrow{D}_\mu \varphi) (\bar{t} \gamma^\mu t)$
$\mathcal{O}_{\varphi B}$	$c_{\varphi B}$	$\left(\varphi^\dagger \varphi - \frac{v^2}{2}\right) B^{\mu\nu} B_{\mu\nu}$	$\mathcal{O}_{\varphi Q}^{(1)}$	$c_{\varphi Q}^{(1)}$	$i(\varphi^\dagger \overleftrightarrow{D}_\mu \varphi) (\bar{Q} \gamma^\mu Q)$
$\mathcal{O}_{\varphi W}$	$c_{\varphi W}$	$\left(\varphi^\dagger \varphi - \frac{v^2}{2}\right) W_I^{\mu\nu} W_{\mu\nu}^I$	$\mathcal{O}_{\varphi Q}^{(3)}$	$c_{\varphi Q}^{(3)}$	$i(\varphi^\dagger \overleftrightarrow{D}_\mu \tau_I \varphi) (\bar{Q} \gamma^\mu \tau^I Q)$
			$\mathcal{O}_{\varphi Q}^{(-)}$	$c_{\varphi Q}^{(-)}$	$c_{\varphi Q}^{(1)} - c_{\varphi Q}^{(3)}$
			$\mathcal{O}_{t\varphi}$	$c_{t\varphi}$	$\left(\varphi^\dagger \varphi - \frac{v^2}{2}\right) \bar{Q} t \tilde{\varphi} + \text{h.c.}$

Table 1: Dimension-6 operators \mathcal{O}_i and their associated Wilson Coefficients c_i entering in $gg \rightarrow ZZ, ZH$ and considered in these proceedings. We follow the notation introduced in [5].

We calculated analytical expressions for the helicity amplitudes of $gg \rightarrow ZZ, ZH$ with up to one insertion of a dimension-6 SMEFT operator in Wolfram Mathematica using the FeynCalc [6–8], FeynHelpers [9], Package-X [10] and FeynArts [11] packages, as well as a modified version of the Mathematica package used in [12]. We then studied the high-energy behaviour of the amplitudes in order to establish, for each process, which operators lead to growths with energy and in which helicity configurations.

2. Growing amplitudes in $gg \rightarrow ZZ$

We start by considering ZZ production modified by top and Higgs operators. There are 36 possible helicity combinations for $gg \rightarrow ZZ$, but using the Bose symmetry of the initial state gluons and final state Z s and the fact that all the operators considered are CP-even lead to 10 independent helicity combinations. The operators probed by $gg \rightarrow ZZ$ and considered here can be divided into three categories. First, $O_{\varphi G}$, $O_{\varphi B}$ and $O_{\varphi W}$ modify the bosonic Higgs couplings. Then $O_{\varphi t}$ and $O_{\varphi Q}^{(-)}$ enter in the top- Z interactions and finally $O_{t\varphi}$ modifies the top-Higgs coupling. The growing SMEFT amplitudes are presented in Table 2.

$\lambda_{g_1}, \lambda_{g_2}, \lambda_{Z_1}, \lambda_{Z_2}$	$O_{\varphi G}$	$O_{\varphi B}$	$O_{\varphi W}$	$O_{\varphi t}$	$O_{\varphi Q}^{(-)}$	$O_{t\varphi}$
+, +, +, +	-	$m_t^2 \left[\log\left(\frac{s}{m_t^2}\right) - i\pi \right]^2$	$m_t^2 \left[\log\left(\frac{s}{m_t^2}\right) - i\pi \right]^2$	-	-	-
+, +, -, -	-	$m_t^2 \left[\log\left(\frac{s}{m_t^2}\right) - i\pi \right]^2$	$m_t^2 \left[\log\left(\frac{s}{m_t^2}\right) - i\pi \right]^2$	-	-	-
+, +, 0, 0	$s \frac{v^2}{m_Z^2}$	-	-	$\frac{m_t^2 v^2}{m_Z^2} \left[\log\left(\frac{s}{m_t^2}\right) - i\pi \right]^2$	$\frac{m_t^2 v^2}{m_Z^2} \left[\log\left(\frac{s}{m_t^2}\right) - i\pi \right]^2$	$\frac{m_t v^3}{m_Z^2} \left[\log\left(\frac{s}{m_t^2}\right) - i\pi \right]^2$

Table 2: High energy behaviour of the $gg \rightarrow ZZ$ helicity amplitudes. Only the dependence on dimensionful quantities, such as particle masses and the vev v is given and overall numerical parameters are neglected. The “-” denotes when a helicity amplitude is not growing. $\lambda_{g_1}, \lambda_{g_2}, \lambda_{Z_1}, \lambda_{Z_2}$ represent the polarisation of the two incoming gluons and the two outgoing Z bosons.

The three top operators lead to a logarithmic growth when both Z bosons are longitudinally polarised, while $O_{\varphi B}$ and $O_{\varphi W}$ lead to a similar growth when the two Z bosons are transversely polarised. The strongest growth is observed when the amplitude is modified by $O_{\varphi G}$. This is because this operator induces a direct coupling between the gluons and the Higgs boson and $gg \rightarrow ZZ$ becomes a tree level process which, like the SM triangle diagrams, is only non-zero in the $(++++)$, $(++--)$ and $(++00)$ helicity configurations [13]. The ggH vertex has two powers of momentum which cancel the $1/s$ coming from the Higgs propagator such that the energy behaviour of the diagram is determined by the contraction of the ZZH vertex with the Z polarisation vectors. This contraction tends to a constant when the Z bosons are transverse and to a quadratic growth when the Z bosons are longitudinal, leading to the observed amplitude growth [14].

The different growths appearing in the analytical expressions of the helicity amplitudes can be observed in kinematic distributions. As a representative example, Fig. 1, reproduced from ref. [15], shows the invariant mass distribution of the Z pair modified by $O_{\varphi W}$, $O_{\varphi G}$ and $O_{\varphi t}$. The distributions for the first two operators are obtained by setting $c/\Lambda^2 = 1 \text{ TeV}^{-2}$. For both $O_{\varphi W}$ and $O_{\varphi G}$, the squared contributions to the total cross-section become larger in the tail of the distribution compared to the threshold region. We note that this growth is more pronounced for $O_{\varphi G}$ which grows quadratically compared to $O_{\varphi W}$, which grows logarithmically. Finally, the high-energy deviation between the SM and the modified SMEFT distributions can be seen for $O_{\varphi t}$, where we set $c/\Lambda^2 = 3.95 \text{ TeV}^{-2}$, the upper 95% CL marginalised bound coming from global fits of LHC data [16]. Whilst this deviation is not very pronounced, it motivates more detailed studies of this process at the HL-LHC and future colliders.

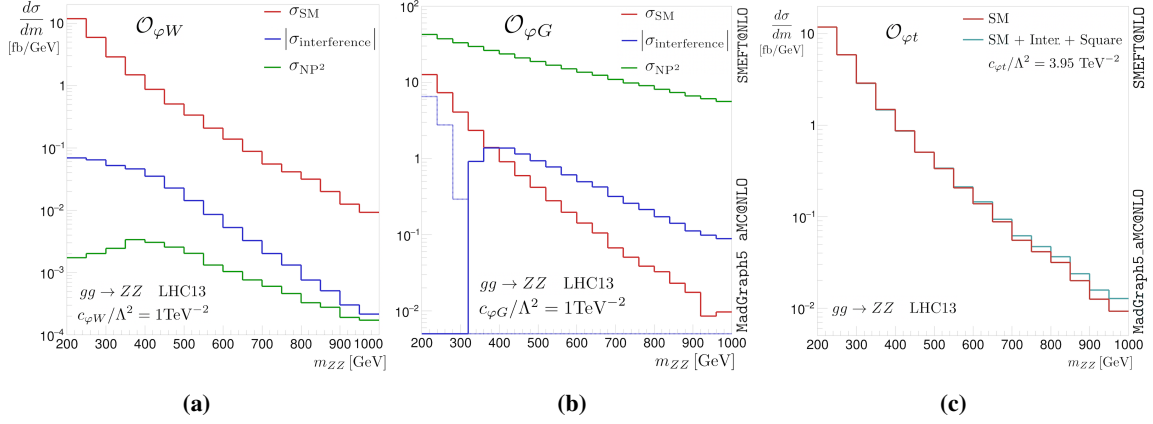


Figure 1: Invariant mass distribution of the Z pair modified by (a) $\mathcal{O}_{\varphi W}$, (b) $\mathcal{O}_{\varphi G}$ and (c) $\mathcal{O}_{\varphi t}$. In (a) and (b), results are shown separately for the SM, the interference between the SM and the new physics, and the new physics squared term. In (c) all three terms are summed to form the light blue line. For the interference, dashed lines denote a negative contribution. Figures (a) and (c) are reproduced from Ref. [15].

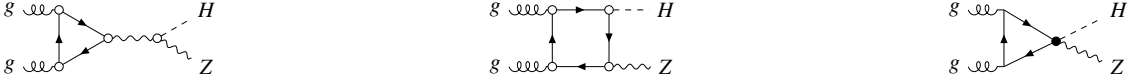


Figure 2: Diagram topologies that enter in the computation of $gg \rightarrow ZH$ in the SMEFT at one-loop for the WCs considered in these proceedings. The empty dots represent couplings that could be either SM-like or modified by dimension-6 operators. The filled dots represent vertices generated only by dimension-6 operators. Only one insertion of dimension-6 operators is allowed per diagram.

3. Growing amplitudes in $gg \rightarrow ZH$

Using the same symmetries as in the previous subsection, we find that there are 5 independent helicity configurations for $gg \rightarrow ZH$. The high energy behaviour of the helicity amplitudes is presented in Table 3 and representative diagrams are shown in Fig. 2. The $t\bar{t}Z$ vertex can be modified by $\mathcal{O}_{\varphi t}$ and $\mathcal{O}_{\varphi Q}^{(-)}$ and these two operators also introduce a $t\bar{t}ZH$ vertex as well as a $b\bar{b}ZH$ one from $\mathcal{O}_{\varphi Q}^{(-)}$. The modified triangle diagrams with a Z propagator and with a $t\bar{t}ZH$ vertex cancel each other exactly, invalidating naive expectations from tree-level $t\bar{t} \rightarrow ZH$ [14]. Given this cancellation, the behaviour of the $\mathcal{O}_{\varphi t}$ and $\mathcal{O}_{\varphi Q}^{(-)}$ amplitudes can be understood from the SM box diagrams with a rescaled $t\bar{t}Z$ interaction. Boxes grow logarithmically in the $(++00)$ helicity configuration and decrease in all other cases. Their growth is not observed in the SM due to the logarithmic terms being exactly cancelled by the triangle diagrams. Both operators therefore lead to a logarithmic growth with energy when the two incoming gluons have the same polarisation and the Z boson is longitudinally polarised. Another consequence of the cancellation between the triangle diagrams with $\mathcal{O}_{\varphi t}$ and $\mathcal{O}_{\varphi Q}^{(-)}$ is that they generate the same behaviour as the Yukawa operator $\mathcal{O}_{t\varphi}$. The latter can only enter in box diagrams with a rescaled $t\bar{t}H$ interaction. Hence, $gg \rightarrow ZH$ is only sensitive to the linear combination $c_{\varphi Q}^{(-)} - c_{\varphi t} + \frac{c_{t\varphi}}{y_t}$, where y_t is the top yukawa. We note that this degeneracy is exact, and does not only hold in the high-energy limit.

$\lambda_{g_1}, \lambda_{g_2}, \lambda_H, \lambda_Z$	$O_{\varphi t}$	$O_{\varphi Q}^{(-)}$	$O_{t\varphi}$
$+, +, 0, 0$	$\frac{m_t^2 v e g_s^2}{32\pi^2 m_Z c_w s_w} \left[\log\left(\frac{s}{m_t^2}\right) - i\pi \right]^2$	$\frac{m_t^2 v e g_s^2}{32\pi^2 m_Z c_w s_w} \left[\log\left(\frac{s}{m_t^2}\right) - i\pi \right]^2$	$\frac{m_t v^2 e g_s^2}{32\sqrt{2}\pi^2 m_Z c_w s_w} \left[\log\left(\frac{s}{m_t^2}\right) - i\pi \right]^2$

Table 3: High energy behaviour of the $gg \rightarrow ZH$ helicity amplitudes. The cosine and the sine of the weak angle are denoted by c_w and s_w and the strong coupling constant is given by g_s .

4. A phenomenology study of $pp \rightarrow ZH$

In this section we assess the sensitivity of $pp \rightarrow ZH$ to dimension-6 SMEFT operators at the HL-LHC. This process consists of a gluon-initiated channel and a quark-induced one, and the interplay between both channels occurs when considering third-generation operators, on which we focus. The quark induced channel enters at tree-level and is sensitive to $O_{\varphi Q}^{(-)}$ and $O_{\varphi Q}^{(3)}$, while the gluon channel is subdominant as it enters at NNLO and is sensitive to $O_{\varphi Q}^{(-)}$, $O_{\varphi t}$ and $O_{t\varphi}$. We added the gluon-initiated signal contribution to an analysis originally focused on quark-initiated diboson production [17] and we relaxed the flavour assumption in said analysis from its original Flavour Universality to $U(2)_q \times U(3)_d \times U(2)_u \times (U(1)_\ell \times U(1)_e)^3$. We simulated the contribution of the $gg \rightarrow ZH$ process using Madgraph5 and SMEFTatNLO [4] at LO in QCD for a centre-of-mass energy of 13 TeV and in the presence of one operator at a time. The collider events are classified into two categories, boosted and resolved, according to the presence of a boosted Higgs candidate or two resolved b -jets respectively. Furthermore, the events are split in two channels according to the number of charged leptons in the final state, either 0 or 2, and a binning in $p_{T,\min} = \min\{p_T^Z, p_T^H\}$ is implemented, but the bin limits are optimised independently for each of the 4 categories.

WC [TeV^{-2}]	95% C.L. Bound (5% syst.)
$c_{\varphi Q}^{(3)}$	[-0.72, 0.57]
$c_{\varphi Q}^{(-)}$	[-1.5, 1.1]
$c_{\varphi t}$	[-8.1, 19.6]
$c_{t\varphi}$	[-19.4, 8.0]

Table 4: Projected bounds at 95% C.L. from one-dimensional fits on the third-generation dimension-6 WCs probed by $pp \rightarrow ZH$ at HL-LHC with integrated luminosity of 3 ab^{-1} . The WCs are in units of TeV^{-2} .

The projected 95% C.L. bounds at the HL-LHC are presented in Table 4. We assume SM-like measurements, uncorrelated observables and a systematic uncertainty of 5%, which is the most realistic assumption for HL-LHC according to current measurements [18]. The operators entering in the quark channel are more constrained than those only probed by the gluon channel. Indeed the quark-induced process enters at tree-level and its contribution to the total cross-section is thus larger than the gluon channel's. The importance of ZH production to probe heavy-quark operators is put in perspective when comparing our projections against current bounds. Global fits of LHC data, including data with luminosity up to 139 fb^{-1} , are able to set bounds $|c_{\varphi Q}^{(3)}| \lesssim 0.6 \text{ TeV}^{-2}$, $|c_{\varphi Q}^{(-)}| \lesssim 2.9 \text{ TeV}^{-2}$ [16]. Our HL-LHC projections for those WCs are similar and slightly better respectively. In the case of $c_{\varphi t}$, LHC data constrain it to $c_{\varphi t} \in [-13.3, 4.0] \text{ TeV}^{-2}$ [16], which is

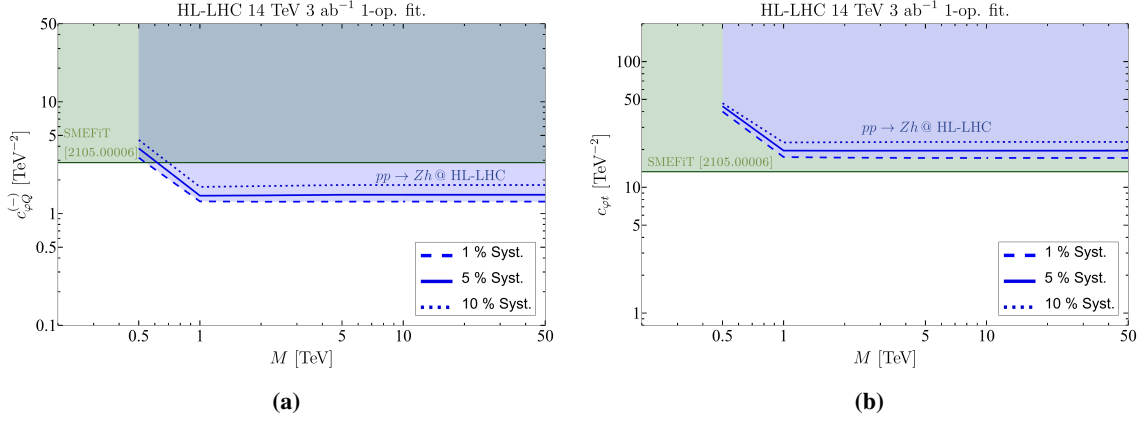


Figure 3: Projected 95% C.L. bounds on (a) $c_{\varphi Q}^{(-)}$ and (b) $c_{\varphi t}$ with different levels of systematic uncertainty at the HL-LHC from a one-operator fit as a function of the maximal-invariant-mass cut M . We also show the bound from the global fit to LHC data performed by the SMEFiT collaboration [16] with a dark green line.

better than the reach of $gg \rightarrow ZH$ at HL-LHC with 5% systematic uncertainty for positive values but worse for negative values. However this process is less competitive to probe $c_{t\varphi}$ since the current bound is $[-2.3, 2.8] \text{ TeV}^{-2}$ [16]. The validity of the EFT description can be assessed by studying the dependence of the bounds on the maximal invariant mass of the ZH system, M . We show it in Fig. 3 for $c_{\varphi Q}^{(-)}$ and $c_{\varphi t}$, where we plot the maximum absolute value of the projected bound. M acts as a proxy for the cutoff of the EFT, hence the bounds in Table 4 are valid as long as the cutoff of the EFT is $\gtrsim 1 \text{ TeV}$, while they degrade significantly for lower cutoffs. In this figure, we also plot the current SMEFiT bound for reference. Overall, ZH production could have a significant impact on future global fits, in particular for $c_{\varphi Q}^{(-)}$, to which it is sensitive thanks to the contributions of both the quark- and gluon-initiated process, and the study presented here motivates differential analyses of $pp \rightarrow ZH$ in future global fits.

5. Conclusion

Diboson production from gluon fusion, namely HH, ZH, ZZ and WW production, are key processes to study multiple Higgs boson properties, and in particular, in the context of the SMEFT, these processes can probe poorly constrained Higgs and top operators as these operators generate growing amplitudes for some helicity configurations. The specific case of $pp \rightarrow ZH$ gives competitive constraints on some third-generation operators which motivates precision measurements of this process in future LHC runs and its inclusion in global fits.

References

- [1] CMS collaboration, *Measurement of the Higgs boson width and evidence of its off-shell contributions to ZZ production*, *Nature Phys.* **18** (2022) 1329 [2202.06923].
- [2] ATLAS collaboration, *Evidence of off-shell Higgs boson production from ZZ leptonic decay channels and constraints on its total width with the ATLAS detector*, *Phys. Lett. B* **846** (2023) 138223 [2304.01532].

- [3] B. Grzadkowski, M. Iskrzynski, M. Misiak and J. Rosiek, *Dimension-Six Terms in the Standard Model Lagrangian*, *JHEP* **10** (2010) 085 [1008.4884].
- [4] C. Degrande, G. Durieux, F. Maltoni, K. Mimasu, E. Vryonidou and C. Zhang, *Automated one-loop computations in the standard model effective field theory*, *Phys. Rev. D* **103** (2021) 096024 [2008.11743].
- [5] A. N. Rossia, M. O. A. Thomas and E. Vryonidou, *Diboson production in the SMEFT from gluon fusion*, 2306.09963.
- [6] R. Mertig, M. Bohm and A. Denner, *FEYN CALC: Computer algebraic calculation of Feynman amplitudes*, *Comput. Phys. Commun.* **64** (1991) 345.
- [7] V. Shtabovenko, R. Mertig and F. Orellana, *New Developments in FeynCalc 9.0*, *Comput. Phys. Commun.* **207** (2016) 432 [1601.01167].
- [8] V. Shtabovenko, R. Mertig and F. Orellana, *FeynCalc 9.3: New features and improvements*, *Comput. Phys. Commun.* **256** (2020) 107478 [2001.04407].
- [9] V. Shtabovenko, *FeynHelpers: Connecting FeynCalc to FIRE and Package-X*, *Comput. Phys. Commun.* **218** (2017) 48 [1611.06793].
- [10] H. H. Patel, *Package-X: A Mathematica package for the analytic calculation of one-loop integrals*, *Comput. Phys. Commun.* **197** (2015) 276 [1503.01469].
- [11] T. Hahn, *Generating Feynman diagrams and amplitudes with FeynArts 3*, *Comput. Phys. Commun.* **140** (2001) 418 [hep-ph/0012260].
- [12] F. Maltoni, L. Mantani and K. Mimasu, *Top-quark electroweak interactions at high energy*, *JHEP* **10** (2019) 004 [1904.05637].
- [13] E. W. N. Glover and J. J. van der Bij, *Z boson pair production via gluon fusion*, *Nucl. Phys. B* **321** (1989) 561.
- [14] A. Azatov, C. Grojean, A. Paul and E. Salvioni, *Resolving gluon fusion loops at current and future hadron colliders*, *JHEP* **09** (2016) 123 [1608.00977].
- [15] A. Azatov et al., *Off-shell Higgs Interpretations Task Force: Models and Effective Field Theories Subgroup Report*, 2203.02418.
- [16] SMEFT collaboration, *Combined SMEFT interpretation of Higgs, diboson, and top quark data from the LHC*, *JHEP* **11** (2021) 089 [2105.00006].
- [17] F. Bishara, P. Englert, C. Grojean, G. Panico and A. N. Rossia, *Revisiting $Vh(\rightarrow b\bar{b})$ at the LHC and FCC-hh*, *JHEP* **06** (2023) 077 [2208.11134].
- [18] ATLAS collaboration, *Combination of measurements of Higgs boson production in association with a W or Z boson in the $b\bar{b}$ decay channel with the ATLAS experiment at $\sqrt{s} = 13$ TeV*, 2021.